ADVANCED OPTICAL MATERIALS
www.advopticalmat.de

High-Performance Photodetector Based on Bi_2Se_3/GeSe Heterojunction with Band Alignment Evolution

Yahui Li, Mengqi Che, Nan Zhang, Yuting Zou, Xingyu Zhao, Yucai Lin, Bingchen Lv, Xiaobao Ma, Yaru Shi, Jianjun Yang, Xiaojuan Sun, Shaojuan Li,* and Dabing Li**

Band alignment engineering in 2D van der Waals heterostructures is a promising method for manufacturing high-speed, high-responsivity, and high-gain photodetectors. Here, a heterojunction photodetector with the band alignment transition from type I to type II under the bias voltage using narrow bandgap material n-Bi_2Se_3 and polarization-sensitive material p-GeSe is designed and prepared. This photodetector possesses excellent performance of broadband detection (532-1550 nm), high responsivity (5.86×10^3 A W^{-1}), high detectivity (1.50×10^{13} Jones), significant external quantum efficiency (1.15×10^6%) and fast response time (97 µs). Compared with the conventional type II band alignment, an additional triangular potential barrier is generated in this type II band alignment evolved from type I. Notably, this triangular barrier will block photogenerated carriers in Bi_2Se_3, which leads to high external quantum efficiency; Furthermore, photogenerated holes can tunnel through this barrier, effectively shortening the response time. Meanwhile, the device can achieve polarization detection (anisotropic ratio = 1.74 at 808 nm) and polarization imaging, which is of great significance for reducing the bit error rate in complex environments.

1. Introduction

Broadband photodetectors are of tremendous research interest owing to their wide potential applications in the fields of optical communications, night vision, medical imaging, security checks, and so on.[1–8] 2D semiconductor materials broke through many limits of traditional materials and became a candidate for the new generation of photoelectric detection materials owing to their wide variety, broad bandgap coverage, and excellent photoelectric properties.[4,9,10] Among them, photodetectors constructed using narrow bandgap 2D materials have been widely studied in the field of broadband photoelectric detection from ultraviolet to terahertz bands.[11–14] Meanwhile, polarized photodetection, as another important factor of photodetection, can effectively reduce the bit error rate by combining the scattering, transmission, and reflection information of objects in complex environments.[15–19] With the continuous improvement of detection accuracy and miniaturization requirements, the introduction of 2D polarization materials with ultra-high carrier mobility, adjustable bandgap, and intrinsic anisotropy has become a new research hotspot in the field of polarization detection and imaging.[20,21] Currently, especially van der Waals heterojunction (vdWH) constructed with 2D materials has attracted widespread attention due to its intriguing properties in combining and exploiting component materials in only one device.[22] Based on this, vdWH photodetectors constructed with narrow-bandgap and polarization-sensitive 2D materials are expected to achieve broadband polarization photodetection.

Due to the 2D vdWH interface with few dangling bonds, it is possible to design heterojunctions with different band alignments.[23–26] In the type I band alignment (straddling), the wider bandgap semiconductor can serve as a potential barrier, trapping carriers in the neighboring narrower bandgap semiconductor. The trapped carriers can act as a local electric field, shifting the Fermi level of the narrower bandgap material, thus inducing more carriers of the opposite type and causing gain of the device.[27,28] For example, Zhang et al. prepared a type I band alignment MoS_2/Ta_2NiSe_5 heterojunction photodetector, which exhibits a high gain of 6×10^7 and a high external quantum efficiency (EQE) of 1.2×10^5% at 532 nm.[12] However, the captured states also cause long response times of 56.4 and 451.2 s at 532 nm, which is a general problem of the gain-time (G-T) tradeoff in 2D materials.[12,29] Besides, the type II band alignments (staggered) can effectively separate carriers under the action of

Y. Li, M. Che, N. Zhang, Y. Zou, X. Zhao, B. Lv, X. Ma, Y. Shi, X. Sun, S. Li, D. Li
State Key Laboratory of Luminescence and Applications
Changchun Institute of Optics
Fine Mechanics and Physics
Chinese Academy of Sciences
Changchun 130033, P. R. China
E-mail: zhangnan@ciomp.ac.cn; lishaojuan@ciomp.ac.cn; lidb@ciomp.ac.cn

Y. Li, M. Che, N. Zhang, Y. Zou, X. Zhao, Y. Lin, B. Lv, X. Ma, Y. Shi, J. Yang, X. Sun, S. Li, D. Li
University of Chinese Academy of Sciences
Beijing 100039, P. R. China

Y. Lin, J. Yang
GPL Photonics Laboratory
State Key Laboratory of Luminescence and Applications
Changchun Institute of Optics, Fine Mechanics and Physics
Chinese Academy of Sciences
Changchun 130033, P. R. China

The ORCID identification number(s) for the author(s) of this article can be found under https://doi.org/10.1002/adom.202302339

DOI: 10.1002/adom.202302339

the electric field, thereby enhancing responsivity (R), and are widely used in photodetectors.[30] For example, Zhai et al. prepared a type II band alignment Bi_2Te_2Se/Bi_2O_2Se heterojunction photodetector, which exhibits a high R of 2210 A W^{-1} at 532 nm under photoconductive and photogating effects.[31] It is worth noting that the band alignment can also be transitioned by the application of an external electric field, in order to effectively integrate the advantages of different band alignments and ultimately achieve performance improvement.[32] Wang et al. used the ultra-high electric field generated by ferroelectric polarization to adjust the band alignment from type II to type I in a $GeSe/MoS_2$ photodetector, where the I_{ph} of type I alignment is nearly tens of times higher than that of type II band alignment.[32] Zhao et al. prepared a Te/In_2S_3 heterojunction photodetector with type II band alignment that can be tuned to type I and type III under positive bias and reverse bias, respectively, resulting in tunable tunneling of photogenerated carriers.[33] When the band alignment changes from type II to type I, the photodetector possesses an R of 146 A W^{-1} and a response time of 5 ms.[33] Notably, the tunneling mechanisms usually improve the response speed of the heterojunction, thus solving the problem of the G-T trade-off in photodetectors. For example, in AsP/InSe and PtS_2/WSe_2 heterostructures, the response times are reduced to 89 and 8 µs under the band-to-band tunneling effect.[22,34] Therefore, it is possible to prepare a photodetector with high R, high EQE, and fast response by combining the precise band alignment design and tunneling mechanisms.

In this work, we conducted a precise band design based on narrow bandgap material n-Bi_2Se_3 and polarization-sensitive material p-GeSe to improve the overall performance of the photodetector. Different from the type I band alignment under zero bias, the band alignment of our device evolves from type I to type II under positive bias with the occurrence of carrier tunneling, effectively combining the advantages of type I (high EQE) and tunneling effect (fast speed). Wherein, the maximum R, detective (D*), and EQE of this photodetector can reach 5.86×10^3 A W^{-1}, 1.50×10^{13} Jones, and 1.15×10^6% at the incident light power of 0.04 mW cm^{-2} at 635 nm. In addition, the photodetector can achieve a 97 µs quick response. Significantly, the device exhibits polarization sensitivity with a polarization ratio of 1.74, and angle-resolved imaging is achieved. The proposed Bi_2Se_3/GeSe heterojunction photodetector holds important application potentials for broadband, high sensitivity, high speed, and polarization photodetection.

2. Results and Discussion

Figure 1a shows the schematic diagram of Bi_2Se_3/GeSe heterojunction photodetector, which is prepared on 285 nm SiO_2/Si substrates. GeSe possesses a "puckered" structure similar to black phosphorus, and Bi_2Se_3 is made up of quintuple layers (QLs) arranged in Se—Bi—Se—Bi—Se subsequences, as shown in Figure 1a.[35,36] The optical microscope image and the Raman spectra of the multilayer Bi_2Se_3, GeSe, and their overlapped heterojunction are shown in Figure S1 (Supporting information). For Bi_2Se_3 (red line), the Raman peaks at 71.35 ($A^1{}_{1g}$) and 174.48 cm^{-1} ($A^2{}_{1g}$) corresponds to out-of-plane vibration modes, and in-plane vibration mode locates at 131.44 cm^{-1} ($E^2{}_g$), respectively.[35,37] For GeSe (blue line), the out-of-plane vibration Raman peaks are located at 81.84 ($A^1{}_{1g}$) and 188.42 cm^{-1} ($A^3{}_g$), and the Raman peak at 150.14 (B_{3g}) corresponds to in-plane vibration mode, respectively.[36,38] In the overlapped heterojunction area (black line), all the above peaks appear in the Raman spectrum, proving the formation of a heterojunction favorably.[39] Figure S1c,d (Supporting Information) display energy dispersive spectroscopy (EDS) spectra of GeSe and Bi_2Se_3, respectively. The element ratios of Ge/Se (1:1) and Bi/Se (2:3) are approximate to their molar ratio. The Se in GeSe is slightly higher than 50%, and the Se in Bi_2Se_3 is slightly lower than 60%, which will cause GeSe and Bi_2Se_3 to show p-type and n-type, respectively. The transfer curves of bare GeSe and bare Bi_2Se_3 in Figure S1e (Supporting Information) again show that GeSe is a p-type semiconductor, while Bi_2Se_3 is a gate voltage-independent material. This is consistent with the reports in previous literatures.[37,40] As shown in Figure S1f (Supporting Information), the thickness of Bi_2Se_3 and GeSe is estimated to be 77 and 54 nm, respectively.

The current–voltage (I_{ds}–V_{ds}) curves at 532–1550 nm with different power densities were measured to determine the photoelectric characteristics of the Bi_2Se_3/GeSe heterojunction photodetector as shown in Figure S2 (Supporting Information). The photodetector possesses obvious current changes under light illumination of different wavelengths. Figure 1b depicts the I_{ds}–V_{ds} curve of the photodetector at 635 nm illumination with varied power. The photocurrent (I_{ph}) increases obviously with the increase of optical power density. Here

$$I_{ph} = I_{light} - I_{dark} \tag{1}$$

where I_{light} and I_{dark} are the light current and the dark current.[28] As shown in the inset of Figure 1b, the output behavior of the device under positive biases can be well-fitted using a Simmons approximation tunnel barrier model, including Fowler–Nordheim (FN) tunneling and direct tunneling. The detailed fitting follows the following formula

$$I_{FNT} \propto V^2 \exp\left(-\frac{4d\sqrt{2m^*\Phi^3}}{3\hbar eV}\right) \tag{2}$$

$$I_{DT} \propto V \exp\left(-\frac{2d\sqrt{2m^*\Phi}}{\hbar}\right) \tag{3}$$

where m^*, d, Φ, and ħ are the effective carrier mass, tunneling thickness, tunneling barrier, and the reduced Planck constant, respectively.[26,41] When small V_{ds} are applied, the curve of $\ln(I/V_{ds}{}^2)$ versus $1/V_{ds}$ exhibits an approximate logarithm relationship. This means that there are carriers that directly tunnel through the interface barrier. As the bias voltage increases, the relationship of $\ln(I/V_{ds}{}^2)$ versus $1/V_{ds}$ shows a negative linear dependence. This means that the direct tunneling would be replaced by the FN tunneling. As shown in Figure 1c, with the aim of displaying the capability of detection and sensitivity of the photodetector, we calculated the R and D* under positive V_{ds}. The R can be derived based on the formula

$$R = \frac{I_{ph}}{P \cdot A} \tag{4}$$

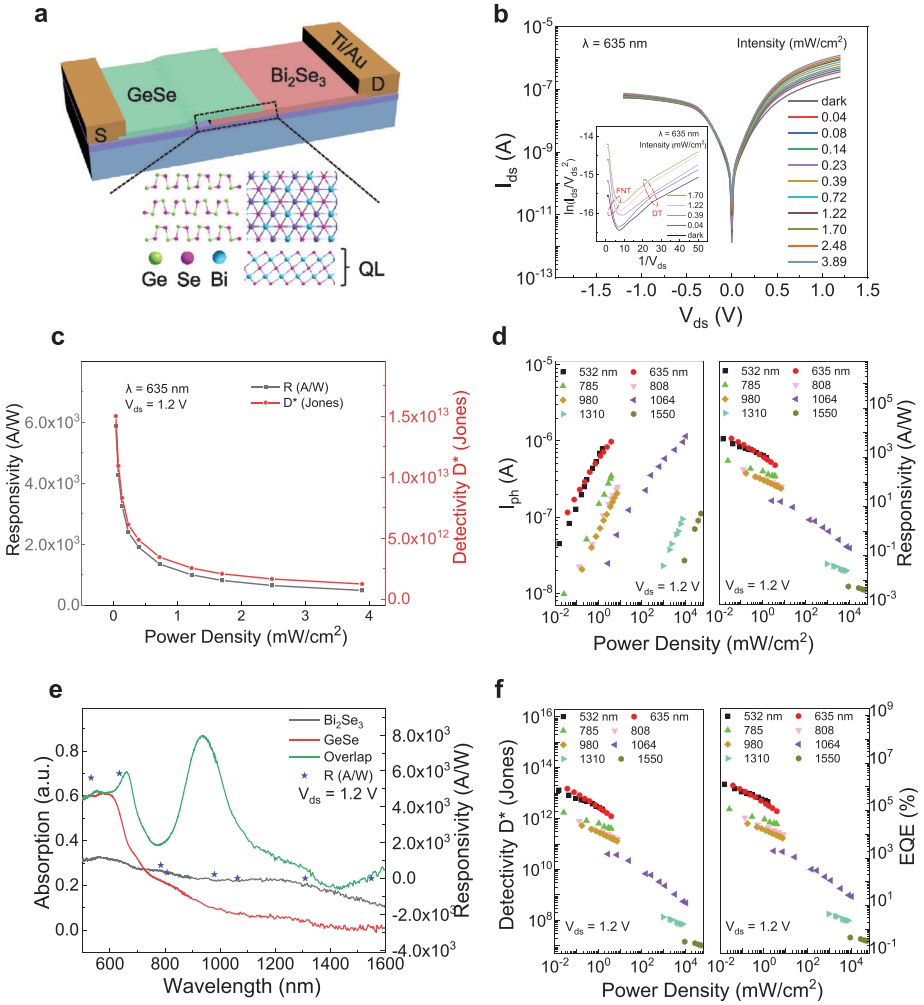

Figure 1. Photoelectric characterization of the Bi_2Se_3/GeSe heterojunction photodetector. a) Schematic diagram of the heterojunction photodetector. b) I_{ds}–V_{ds} characteristic curves. Inset: The curve of ln (I_{ds}/V_{ds}^2) versus $1/V_{ds}$ of the heterojunction photodetector. c) Responsivity and detectivity of the device at 635 nm with different light power densities. d) I_{ph} and responsivity of the photodetector at different wavelengths. e) Absorption spectra of bare Bi_2Se_3, GeSe, and their overlapped heterojunction transferred to sapphire substrate. f) Detectivity and EQE of the heterojunction photodetector at different wavelengths.

where P and A are the incident light power density and the effective photosensitive area of the heterojunction.[28] The R is 5.86 × 10^3 A W^{-1} measured at the incident light power of 0.04 mW cm^{-2} at 635 nm and it decreases with promoting the optical power density due to the saturation of I_{ph} at higher power. The bias-dependent response characteristics of the photodetector at different wavelengths are shown in Figure S3 (Supporting Information), which demonstrates that R increases as V_{ds} increases, and the value of R under positive bias is higher than that under negative bias. The

$$D^* = \frac{I_{ph} \cdot A^{1/2}}{P \cdot A \cdot \left(2eI_{dark}\right)^{1/2}} = R \cdot \frac{A^{1/2}}{\left(2eI_{dark}\right)^{1/2}} \quad (5)$$

is another key parameter that characterizes the device photoresponse property, where e is the elementary charge.[22,28] As shown in Figure 1c, the maximum D* is 1.50 × 10^{13} Jones measured at the incident light power of 0.04 mW cm^{-2} at 635 nm. Figure 1d depicts the plots of I_{ph} and calculated R at V_{ds} = 1.2 V with varied optical power density at different wavelengths. The I_{ph} increases with the increase of optical power density, whereas R decreases as increasing the optical power density. It is worth noting that the wavelength-dependent R generally follows the absorption spectrum, as shown in Figure 1e. When the device is irradiated by light of a longer wavelength beyond ≈1000 nm, Bi_2Se_3 becomes the main light absorption material to generate photogenerated carriers, yielding a smaller photoresponse. Figure 1f shows the power-dependent D* and EQE at different wavelengths. The D* also increases under higher optical power density. As for EQE

$$EQE = \frac{hc}{e\lambda}R \quad (6)$$

where h, c, and λ correspond to the Planck constant, speed of light, and wavelength of incident light, respectively.[28] As

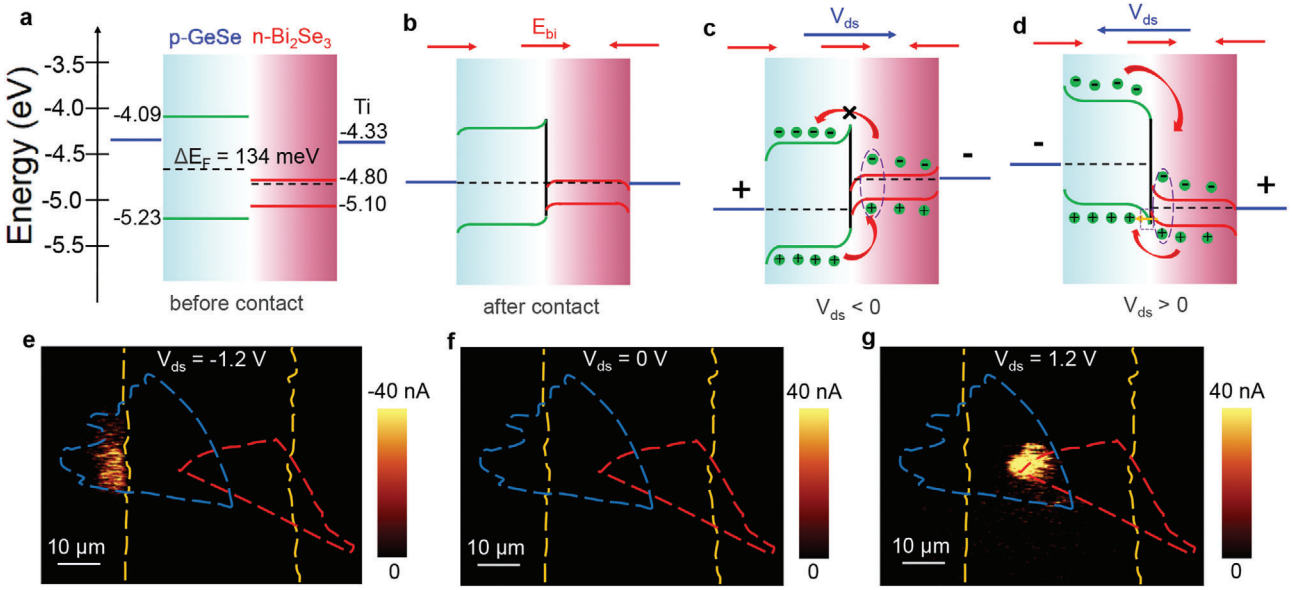

Figure 2. Working mechanisms of the Bi_2Se_3/GeSe heterojunction photodetector. a,b) Band diagram of GeSe and Bi_2Se_3 before and after contact, respectively. c,d) Band diagrams of the Bi_2Se_3/GeSe heterojunction photodetector at $V_{ds} < 0$ and $V_{ds} > 0$, respectively. Red arrow: built-in electric field; Blue arrow: source-drain electric field; Orange arrow: F–N tunneling; Purple dashed ellipse: photocarriers recombination; Purple dashed rectangle: tunneling barrier. e–g) Photocurrent mappings of the Bi_2Se_3/GeSe heterostructure device under different bias conditions with V_{ds} of −1.2, 0, and 1.2 V. The incident light is 633 nm. The blue, red, and yellow dashed lines illustrate the outlines of GeSe, Bi_2Se_3, and metal electrodes, respectively.

shown in Figure 1f, the maximum EQE of this photodetector is 1.15 × 10^6% measured at the incident light power of 0.04 mW cm^{-2} at 635 nm. The high value of EQE indicates the strong photoelectric conversion capability of this photodetector and high internal gain.[12] As shown in Figure S4 (Supporting Information), the characteristics of EQE-V_{ds} at different wavelengths show a consistent trend with R-V_{ds} of the device. EQE increases with the increase of V_{ds}, and the value of EQE under positive bias is higher than that under negative bias. For better comparison, the I_{ds}–V_{ds} curves of the bare GeSe photodetector at 635 nm with different power densities were also measured. As shown in Figure S5 (Supporting Information), the R and EQE of the Bi_2Se_3/GeSe heterojunction photodetector are two orders of magnitude higher than that of the bare GeSe photodetector.

In order to explore the optical response mechanism, the surface potential of Bi_2Se_3/GeSe heterojunction was measured by Kelvin Probe Force Microscopy (KPFM).[22] As shown in Figure S6 (Supporting Information), the surface potential difference of these two materials corresponds to the Fermi level difference, which is approximately confirmed as 134 meV. According to previous literatures, the conduction band minimum and the valence band maximum of Bi_2Se_3 (GeSe) are ≈−4.80 eV (−4.09 eV) and −5.10 eV (−5.23 eV).[35,37,38,42] The offsets of the conduction and valence band between these two materials are ≈0.71 and 0.13 eV, respectively. The energy band profiles of Ti, GeSe, and Bi_2Se_3 before contact are shown in **Figure 2a**, where a type I band alignment is formed.[43] Owing to the difference in Fermi energy level, the electrons of GeSe move into Bi_2Se_3, and finally reach an equilibrium state. Naturally, a bilateral accumulation region will be formed at the interface, and a built-in electric field will also be formed from GeSe to Bi_2Se_3.[44] As shown in Figure 2b, the energy band near the GeSe surface tends to bend downward, while the energy band near the Bi_2Se_3 surface bends upward. Considering the work function of metal Ti contact, Schottky and Ohmic contacts are formed on the GeSe and Bi_2Se_3 sides, respectively.[43]

As shown in Figure 2c, when $V_{ds} < 0$ is applied to the photodetector, the band bending of the two materials increases, which increases the potential barrier for the electrons in the Bi_2Se_3 side to enter GeSe, resulting in the accumulation of a large number of electrons on the Bi_2Se_3 side. When both GeSe and Bi_2Se_3 generate photogenerated carriers, the photogenerated holes in GeSe enter n-Bi_2Se_3 under the action of the electric field. However, these photoexcited holes are prone to recombine with the intrinsic majority carrier (electrons) in n-Bi_2Se_3 and the accumulated electrons blocked by conduction band barriers in Bi_2Se_3, making it difficult to reach the drain electrode. Meanwhile, the photoexcited electrons on Bi_2Se_3 side were blocked by the conduction band offset and could not drive to the GeSe side to generate I_{ph}, and only the photogenerated electrons in GeSe are collected by the source electrode, leading to a small I_{ph} as illustrated in Figure 2e.[43]

As shown in Figure 2d, when $V_{ds} > 0$ is applied, the band bending will reverse and the band alignment will also change from type I to type II, which is more conducive to carrier separation. It should be emphasized that in this type II band alignment, there is an additional triangular barrier caused by the valence band offset of the constituted materials. Part of the photogenerated holes of Bi_2Se_3 will be blocked by the triangular barrier. The trapped holes induce electric field-effect which will shift the Fermi level, inducing the generation of a large number of electrons and causing gain.[27,28] Another part of the photogenerated holes will tunnel through this triangular barrier under the action of the tunneling mechanism, which will cause a fast response. The photogenerated electrons in the entire device will transport across n-Bi_2Se_3

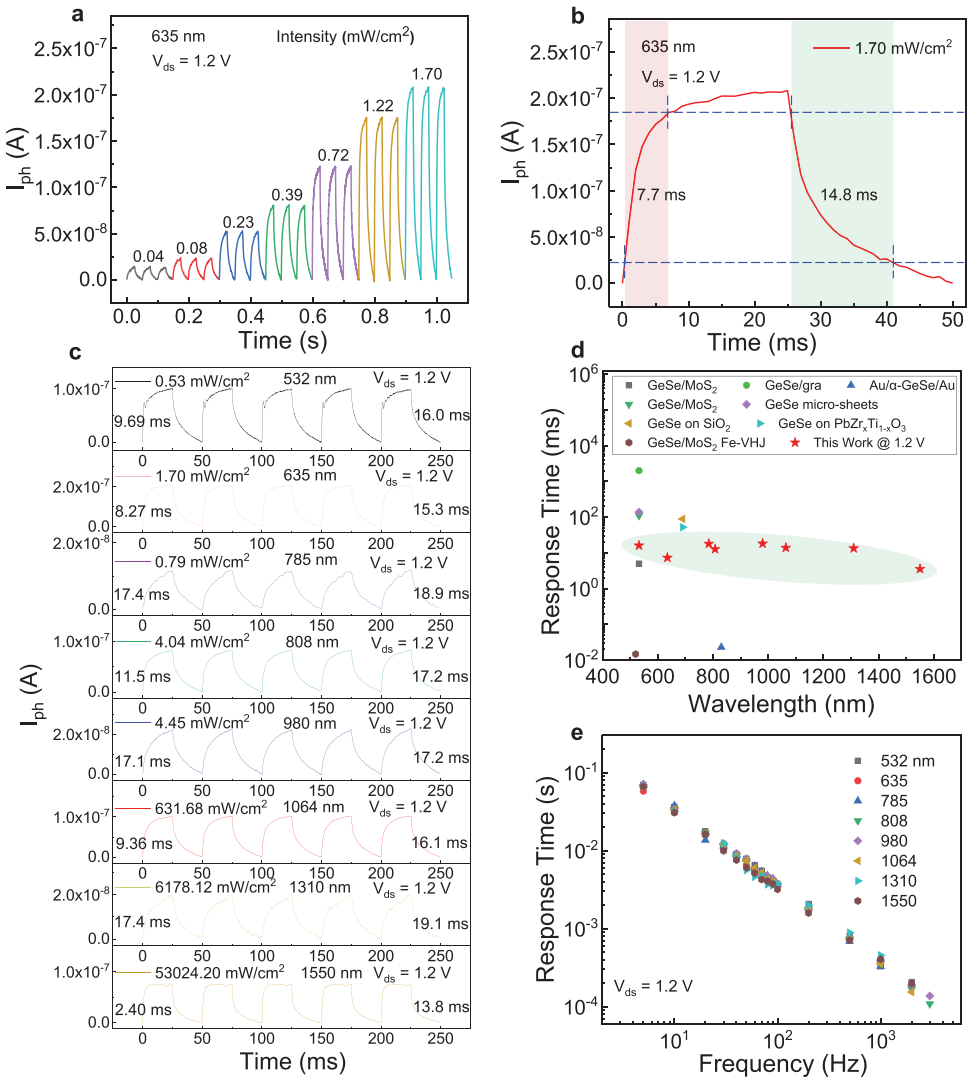

Figure 3. The time-dependent optical responses of the Bi_2Se_3/GeSe heterojunction photodetector. a) Time-dependent optical responses of the heterojunction photodetector at 635 nm with different power densities. b) Rise time and fall time of the heterojunction photodetector at 1.2 V. c) Time-dependent optical responses at different wavelengths with 20 Hz. d) Comparison of the response time of GeSe-based photodetectors with our results. e) Response time at different wavelengths with modulated light frequency.

with electrons as the majority carriers to the drain electrode. The photogenerated holes that tunnel into GeSe and in GeSe will transport across by p-GeSe to the source electrode. Therefore, the device possesses higher I_{ph} (Figure S2, Supporting Information), high R (Figure S3, Supporting Information), and high EQE (Figure S4, Supporting Information) under positive bias voltage.

The above analyses are consistent with the photocurrent mapping results shown in Figure 2e–g. When V_{ds} = −1.2 V, I_{ph} is mainly generated near the source electrode, while as for V_{ds} = 0 V, there is no significant I_{ph} generation, which is due to the lack of self-driving effect, resulting in the photogenerated electrons in GeSe may recombine with majority carrier, holes, in p-GeSe, and failed to be collected by the source electrode in time. The photocurrent mapping result at 0 V is consistent with the I_{ds}–V_{ds} characteristic curve result as well (Figure 1b). However, when V_{ds} = 1.2 V, the type II band alignment effectively separates the photogenerated carriers, so the I_{ph} is mainly generated in the junction region, which is consistent with our analysis in Figure 2d.

The time-dependent optical responses of the photodetector at 532–1550 nm were measured under different light power densities. **Figure 3**a shows the optical switching characteristics at 635 nm under different incident light power densities. As displayed in Figure 3b, the rise time and fall time measured to be 7.7 and 14.8 ms with 20 Hz modulation frequency. Here, the rise (fall) time is defined as the time from 10% to 90% (from 90% to 10%) of the maximum current value, respectively.[12] Figure S7 (Supporting Information) presents optical switching characteristics under different incident light power densities, and we notice that high incident light power density can shorten response time to some extent. The optical switching characteristics at the above wavelengths with 20 Hz modulation frequency

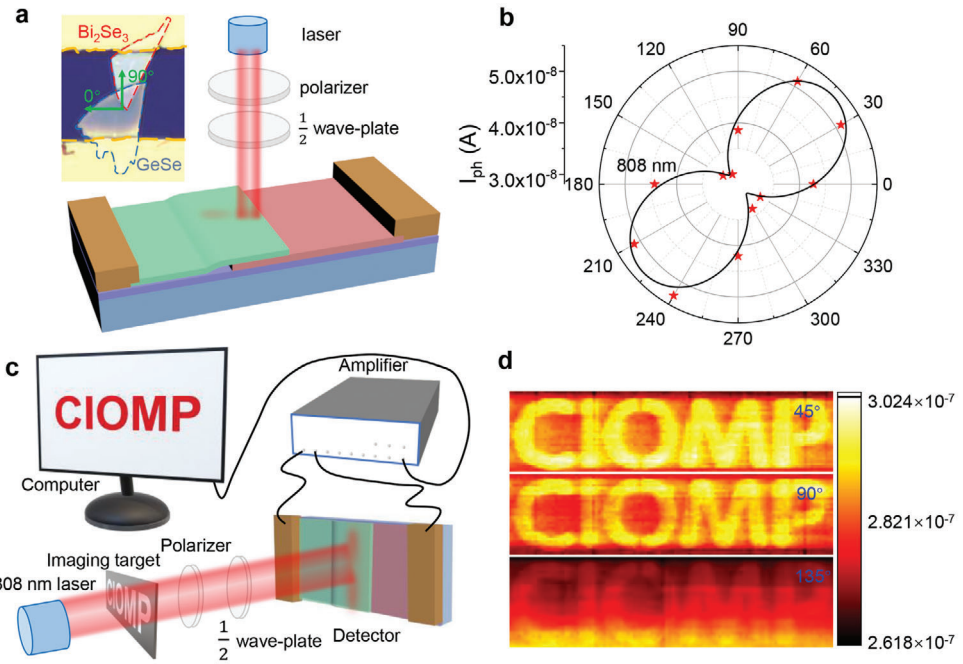

Figure 4. Polarization-sensitive photodetection of the Bi_2Se_3/GeSe heterojunction photodetector. a) Schematics of the experimental setup for polarization measurement. b) The polarized photocurrent at 808 nm at 1.2 V bias voltage. c) Schematics of the experimental setup for polarization-sensitive imaging measurement. d) Imaging of "CIOMP" letter with different polarization angles of incident light.

are illustrated in Figure 3c. The optical switching characteristics reflect that this photodetector possesses a stable and repeatable optical response in a wide band. Figure 3d presents the comparison of the response time between our device and previous reports, and it is found that the response speed of this device is relatively fast.[21,32,45–49] In addition, the bare GeSe device was also tested under the same conditions, and it is not difficult to find that the response time of this Bi_2Se_3/GeSe heterojunction photodetector is slightly shorter than that of the bare GeSe device (Figure S8, Supporting Information). The rapid response of this Bi_2Se_3/GeSe heterojunction photodetector can be attributed to the tunneling behavior of the heterojunction interface as shown in Figure 2. The device can respond to light with a high modulation frequency of up to 3000 Hz, with the shortest response time of the device reaching 97 µs (Figure S9, Supporting Information). As depicted in Figure 3e, the modulation frequency can affect the response time, which varies from tens of ms to tens of µs. The general trend is that the response time decreases with the increase of modulation frequency.[6,50,51] To further illustrate the high performance of our device, Table S1 (Supporting Information) lists the comparison of the performance parameters of our work with other GeSe-based photodetectors.[21,32,41,45,46,48,49] Notably, the Bi_2Se_3/GeSe heterojunction photodetector possesses excellent overall performance, holding application potential for high-performance broadband photodetection.

Furthermore, the polarization-sensitive photodetector can detect the polarization information of the injected light with an improved signal-to-noise ratio, thus expanding the amount of information obtained and reducing the error rate.[21] For polarization-resolved I_{ph} measurement, the schematic diagram of the experimental setup is shown in **Figure** 4a. The polarization-resolved I_{ph} of the device is measured at V_{ds} = 1.2 V. Figure 4b and Figure S10 (Supporting Information) show the polarization-resolved I_{ph} curves of the photodetector at infrared wavelengths. Obviously, the polarization-dependent photocurrent varies periodically as the polarization angle changes from 0° to 360°. It can be found that the I_{ph} reaches the maximum value at 45° (225°), and reaches the minimum value when the polarization angle is at 135° (315°). The anisotropy of I_{ph} is caused by the anisotropy of the light absorption of GeSe.[52,53] In addition, the anisotropic ratios are 1.66, 1.74, 1.58, and 1.58 at 785, 808, 980, and 1064 nm wavelengths, respectively, which are comparable with previously reported GeSe-based photodetector (Table S2, Supporting Information).[21,32,49,52] Therefore, the introduction of polarization-sensitive material GeSe endows the device with the ability to detect the polarization state of incident light.

In order to further explore the possibility of the polarization infrared image sensing capability of the Bi_2Se_3/GeSe heterojunction photodetector, the polarization-sensitive imaging measurement of the device is conducted, and the schematic diagram is shown in Figure 4c. The photograph of the experimental setup mentioned above is illustrated in Figure S11 (Supporting Information). A hollow pattern of the letters "CIOMP" as a mask is located by a 2D rotary table and this mask is set between the light source and the lens. As shown in Figure 4d, the obvious shapes of "CIOMP" can be observed at 808 nm. The shape is clearest when the polarization angle is 45°, and it is the least clear at 135°. The clarity of the shape reflects the magnitude of the I_{ph}. Obviously, Figure 4b,d shows consistent angle-dependence characteristics. The polarization detection and polarization imaging ability, as well as remarkable R and pronounced

D*, indicate the Bi_2Se_3/GeSe heterojunction photodetector possesses a high prospect for future photoelectric devices and optical applications.

3. Conclusion

In summary, we prepared a broadband polarization photodetector using narrow bandgap material Bi_2Se_3 and polarization-sensitive material GeSe. The band alignment of the Bi_2Se_3/GeSe photodetector can be tuned from type I to type II under positive bias voltage. Notably, this photodetector not only retains the advantage of high EQE in type I band alignment, but also possesses the advantages of fast response under the tunneling mechanism. The maximum R of this photodetector can reach 10^3 A W^{-1} in the visible band, and 10^2 A W^{-1} in the near-infrared band. The fastest response time of this photodetector reaches 97 µs. The polarization ratio can achieve 1.74 at 808 nm. In addition, this photodetector can be integrated into polarization imaging systems, showing polarization imaging capability. The precise band design of vdWH provides a novel platform for the design and preparation of efficient photodetectors in the future.

4. Experimental Section

Device Fabrication: Bi_2Se_3 and GeSe flakes were mechanically exfoliated from their bulk single crystals (sixCarbon Technology Shenzhen, China) by using scotch tape. The flakes used were thinned by repeatedly folding the tape and transferred to Polydimethylsiloxane (PDMS) film (METATEST Corporation, China), respectively. Then, multilayer Bi_2Se_3 and GeSe flakes on PDMS with moderate thickness, large size, flat, and clean surfaces were selected under the optical microscope (Nikon Corporation, Japan). The Bi_2Se_3 flake, as the bottom material of heterojunction, was transferred onto precleaned Si/SiO_2 (285 nm) substrate by PDMS using a high-precision 2D material transfer platform (METATEST Corporation, China, E1-T). Next, the GeSe flake, as the top material of the heterojunction, was transferred to one side of the Bi_2Se_3 flake using the method mentioned above, and the Bi_2Se_3/GeSe heterojunction was successfully fabricated. The metal electrodes were patterned by UV-lithography. Subsequently, 10 nm Ti and 80 nm Au were deposited on both Bi_2Se_3 and GeSe following with a lift-off process. For optical absorption measurements, the Bi_2Se_3 and GeSe flakes were transferred onto precleaned double-polished sapphire substrate. For the EDS test, Bi_2Se_3 and GeSe flakes with a thickness of µm were transferred to low resistant silicon substrate.

Electrical and Photoelectrical Measurements: The morphology of Bi_2Se_3/GeSe heterojunction was characterized by optical microscopy (Nikon Corporation, Japan). AFM and KPFM images of the Bi_2Se_3/GeSe heterojunction were obtained by atomic force microscope (Oxford Instruments, Britain, Cypher S). In order to identify the quality of the exfoliated flakes, the Raman spectra were performed by high-resolution Raman spectrometer with a 532 nm excitation laser (Horiba Scientific, France, LabRAM HR Evolution). Photocurrent mapping measurements were also conducted by the above-mentioned Raman spectrometer with a 633 nm excitation laser. In order to explore the composition of these two materials, the EDS spectra were tested by an energy spectrometer (Hitachi Limited, Japan, S4800). The relatively photoelectrical measurements of the Bi_2Se_3/GeSe heterojunction photodetector were performed by a semiconductor analyzer (METATEST Corporation, China, Metatest E2) at room temperature. The photoelectrical properties were measured under 532, 635, 785, 808, 980, 1064, 1310, and 1550 nm laser beams with a diameter ≈50 µm, respectively.

Supporting Information

Supporting Information is available from the Wiley Online Library or from the author.

Acknowledgements

This work is supported by the Science Fund for Creative Research Groups of the National Natural Science Foundation of China (Grant No. 62121005), the National Key Research and Development Program (Grant No. 2021YFA 0717600), the National Natural Science Foundation of China (Grant No. 62022081, 62334010 , 61974099 and 62304221), the Natural Science Foundation of Jilin Province (Grant No. 20220508030RC), Changchun Key Research and Development Program (Grant No. 21ZY03), China Postdoctoral Science Foundation (2021TQ0358 and 2021M703128).

Conflict of Interest

The authors declare no conflict of interest.

Data Availability Statement

The data that support the findings of this study are available from the corresponding author upon reasonable request.

Keywords

2D heterojunction, band alignment, broadband, polarization imaging

Received: September 20, 2023
Revised: November 21, 2023
Published online: December 17, 2023

[1] B. N. Shivananju, X. Z. Bao, W. Z. Yu, J. Yuan, H. Mu, T. Sun, T. Y. Xue, Y. P. Zhang, Z. Z. Liang, R. F. Kan, H. Zhang, B. Lin, S. J. Li, Q. L. Bao, *Adv. Funct. Mater.* **2019**, *29*, 1807274.
[2] C. Shu, N. Zhang, Y. Y. Gao, J. R. An, X. Wen, W. L. Ma, Z. K. Liu, B. Q. Sun, S. J. Li, *ACS Appl. Mater. Interfaces* **2022**, *14*, 24648.
[3] G. Wang, M. Zhang, D. Chen, Q. L. Guo, X. F. Feng, T. C. Niu, X. S. Liu, A. Li, J. W. Lai, D. Sun, Z. M. Liao, Y. Q. Wang, P. K. Chu, G. Q. Ding, X. M. Xie, Z. F. Di, X. Wang, *Nat. Commun.* **2018**, *9*, 5168.
[4] W. Ahmad, J. Wu, Q. D. Zhuang, A. Neogi, Z. M. Wang, *Small* **2023**, *19*, e2207641.
[5] A. Li, Q. X. Chen, P. P. Wang, Y. Gan, T. L. Qi, P. Wang, F. D. Tang, J. Z. Wu, R. Chen, L. Y. Zhang, Y. P. Gong, *Adv. Mater.* **2019**, *31*, 1805656.
[6] J. Bullock, M. Amani, J. Cho, Y.-Z. Chen, G. H. Ahn, V. Adinolfi, V. R. Shrestha, Y. Gao, K. B. Crozier, Y.-L. Chueh, A. Javey, *Nat. Photonics* **2018**, *12*, 601.
[7] L. H. Zeng, W. Han, X. Y. Ren, X. Li, D. Wu, S. J. Liu, H. Wang, S. P. Lau, Y. H. Tsang, C. X. Shan, J. S. Jie, *Nano Lett.* **2023**, *23*,8241.
[8] Y. P. Wu, S. E. Wu, J. J. Hei, L. H. Zeng, P. Lin, Z. F. Shi, Q. M. Chen, X. J. Li, X. C. Yu, D. Wu, *Nano Res.* **2023**, *16*, 11422.
[9] F. H. L. Koppens, T. Mueller, P. Avouris, A. C. Ferrari, M. S. Vitiello, M. Polini, *Nat. Nanotechnol.* **2014**, *9*, 780.
[10] A. Jakhar, P. Kumar, A. Moudgil, V. Dhyani, S. Das, *Adv. Opt. Mater.* **2020**, *8*, 1901714.
[11] H. Z. Gul, W. Sakong, H. Ji, J. Torres, H. Yi, M. K. Ghimire, J. H. Yoon, M. H. Yun, H. R. Hwang, Y. H. Lee, S. C. Lim, *ACS Appl. Mater. Interfaces* **2019**, *11*, 19565.

[12] T. Guo, X. Song, P. Wei, J. Li, Y. Gao, Z. Cheng, W. Zhou, Y. Gu, X. Chen, H. Zeng, S. Zhang, *ACS Appl. Mater. Interfaces* **2022**, *14*, 56384.
[13] X. W. Guan, X. C. Yu, D. Periyanagounder, M. R. Benzigar, J. K. Huang, C. H. Lin, J. Kim, S. Singh, L. Hu, G. Z. Liu, D. H. Li, J. H. He, F. Yan, Q. J. Wang, T. Wu, *Adv. Opt. Mater.* **2020**, *9*, 2001708.
[14] H.-K. Jo, J. Kim, Y. R. Lim, S. Shin, D. S. Song, G. Bae, Y. M. Kwon, M. Jang, S. Yim, S. Myung, S. S. Lee, C. G. Kim, K. K. Kim, J. Lim, W. Song, *ACS Nano* **2023**, *13*, 1372.
[15] L. H. Zeng, Q. M. Chen, Z. X. Zhang, D. Wu, H. Yuan, Y. Y. Li, W. Qarony, S. P. Lau, L. B. Luo, Y. H. Tsang, *Adv. Sci.* **2019**, *6*, 1901134.
[16] J. W. Lai, X. Liu, J. C. Ma, Q. S. Wang, K. N. Zhang, X. Ren, Y. N. Liu, Q. Q. Gu, X. Zhuo, W. Lu, Y. Wu, Y. Li, J. Feng, S. Y. Zhou, J.-H. Chen, D. Sun, *Adv. Mater.* **2018**, *30*, 1707152.
[17] X. N. Han, P. T. Wen, L. Zhang, W. Gao, H. Y. Chen, F. Gao, S. H. Zhang, N. J. Huo, B. S. Zou, J. B. Li, *ACS Appl. Mater. Interfaces* **2021**, *13*, 61544.
[18] J. Qiao, F. Feng, Z. M. Wang, M. Y. Shen, G. P. Zhang, X. C. Yuan, M. G. Somekh, *ACS Appl. Mater. Interfaces* **2021**, *13*, 17948.
[19] J. Ahn, K. Ko, J.-H. Kyhm, H.-S. Ra, H. Bae, S. Hong, D. Y. Kim, J. Jang, T. W. Kim, S. Choi, J.-H. Kang, N. Kwon, S. Park, B.-K. Ju, T.-C. Poon, M.-C. Park, S. Im, D. K. Hwang, *ACS Nano* **2021**, *15*, 17917.
[20] D. Wu, M. M. Xu, L. H. Zeng, Z. F. Shi, Y. Z. Tian, X. J. Li, C. X. Shan, J. S. Jie, *ACS Nano* **2022**, *16*, 5545.
[21] Y. Xin, X. X. Wang, Z. Chen, D. Weller, Y. Y. Wang, L. J. Shi, X. Ma, C. J. Ding, W. Li, S. Guo, R. B. Liu, *ACS Appl. Mater. Interfaces* **2020**, *12*, 15406.
[22] F. Wu, H. Xia, H. D. Sun, J. W. Zhang, F. Gong, Z. Wang, L. Chen, P. Wang, M. S. Long, X. Wu, J. L. Wang, W. C. Ren, X. S. Chen, W. Lu, W. D. Hu, *Adv. Funct. Mater.* **2019**, *29*, 1900314.
[23] Z. H. Wang, H. Zhang, W. K. Wang, C. Y. Tan, J. W. Chen, S. Q. Yin, H. L. Zhang, A. K. Zhu, G. Li, Y. C. Du, S. T. Wang, F. G. Liu, L. Li, *ACS Appl. Mater. Interfaces* **2022**, *14*, 37926.
[24] J. Zhang, J. H. Wang, P. Chen, Y. Sun, S. Wu, Z. Y. Jia, X. B. Lu, H. Yu, W. Chen, J. Q. Zhu, G. B. Xie, R. Yang, D. X. Shi, X. B. Xu, J. Y. Xiang, K. H. Liu, G. Y. Zhang, *Adv. Mater.* **2016**, *28*, 1950.
[25] P. K. Srivastava, Y. Hassan, Y. Gebredingle, J. Jung, B. Kang, W. J. Yoo, B. Singh, C. Lee, *Small* **2019**, *15*, 1804885.
[26] Z. T. Luo, H. K. Xu, W. Gao, M. M. Yang, Y. He, Z. H. Huang, J. D. Yao, M. L. Zhang, H. F. Dong, Y. Zhao, Z. Q. Zheng, J. B. Li, *Small* **2023**, *19*, 2207615.
[27] R. Nur, T. Tsuchiya, K. Toprasertpong, K. Terabe, S. Takagi, M. Takenaka, *Commu. Mater.* **2020**, *1*, 103.
[28] M. Buscema, J. O. Island, D. J. Groenendijk, S. I. Blanter, G. A. Steele, H. S. J. van der Zant, A. Castellanos-Gomez, *Chem. Soc. Rev.* **2015**, *44*, 3691.
[29] N. Guo, L. Xiao, F. Gong, M. Luo, F. Wang, Y. Jia, H. C. Chang, J. K. Liu, Q. Li, Y. Wu, Y. Wang, C. X. Shan, Y. Xu, P. Zhou, W. D. Hu, *Adv. Sci.* **2019**, *7*, 1901637.
[30] A. Varghese, D. Saha, K. Thakar, V. Jindal, S. Ghosh, N. V. Medhekar, S. Ghosh, S. Lodha, *Nano Lett.* **2020**, *20*, 1707.
[31] S. J. Yang, P. Luo, F. K. Wang, T. Liu, Y. H. Zhao, Y. Ma, H. Q. Li, T. Y. Zhai, *Small* **2022**, *18*, 2105211.
[32] Y. Chen, X. D. Wang, L. Huang, X. T. Wang, W. Jiang, Z. Wang, P. Wang, B. M. Wu, T. Lin, H. Shen, Z. M. Wei, W. D. Hu, X. J. Meng, J. H. Chu, J. L. Wang, *Nat. Commun.* **2021**, *12*, 4030.
[33] X. H. Cao, Z. H. Lei, B. Q. Huang, A. X. Wei, L. L. Tao, Y. B. Yang, Z. Q. Zheng, X. Feng, J. B. Li, Y. Zhao, *Small* **2022**, *18*, 2200445.
[34] C. Y. Tan, S. Q. Yin, J. W. Chen, Y. Lu, W. S. Wei, H. F. Du, K. L. Liu, F. K. Wang, T. Y. Zhai, L. Li, *ACS Nano* **2021**, *15*, 8328.
[35] H. B. Zhang, X. J. Zhang, C. Liu, S.-T. Lee, J. S. Jie, *ACS Nano* **2016**, *10*, 5113.
[36] W. C. Yap, Z. F. Yang, M. Mehboudi, J.-A. Yan, S. Barraza-Lopez, W. J. Zhu, *Nano Res.* **2017**, *11*, 420.
[37] M. Yu, C. C. Fang, J. F. Han, W. L. Liu, S. M. Gao, K. Huang, *ACS Appl. Mater. Interfaces* **2022**, *14*, 13507.
[38] X. Zhou, X. Z. Hu, B. Jin, J. Yu, K. L. Liu, H. Q. Li, T. Y. Zhai, *Adv. Sci.* **2018**, *5*, 1800478.
[39] Y. Chen, X. D. Wang, G. J. Wu, Z. Wang, H. H. Fang, T. Lin, S. Sun, H. Shen, W. D. Hu, J. L. Wang, J. L. Sun, X. J. Meng, J. H. Chu, *Small* **2018**, *14*, 1703293.
[40] H. Q. Zhao, Y. L. Mao, X. Mao, X. Shi, C. S. Xu, C. X. Wang, S. M. Zhang, D. H. Zhou, *Adv. Funct. Mater.* **2017**, *28*, 1704855.
[41] Z. Y. Yang, B. Jiang, Z. J. Zhang, Z. Z. Wang, X. B. He, D. Wan, X. M. Zou, X. Q. Liu, L. Liao, F. K. Shan, *Appl. Phys. Lett.* **2020**, *116*, 141101.
[42] Z. Y. Yang, L. Liao, F. Gong, F. Wang, Z. Wang, X. Q. Liu, X. H. Xiao, W. D. Hu, J. He, X. F. Duan, *Nano Energy* **2018**, *49*, 103.
[43] H. Xue, Y. D. Wang, Y. Y. Dai, W. Kim, H. Jussila, M. Qi, J. Susoma, Z. Y. Ren, Q. Dai, J. L. Zhao, K. Halonen, H. Lipsanen, X. M. Wang, X. T. Gan, Z. P. Sun, *Adv. Funct. Mater.* **2018**, *28*, 1804388.
[44] F. Wu, Q. Li, P. Wang, H. Xia, Z. Wang, Y. Wang, M. Luo, L. Chen, F. S. Chen, J. S. Miao, X. S. Chen, W. Lu, C. X. Shan, A. L. Pan, X. Wu, W. C. Ren, D. Jariwala, W. D. Hu, *Nat. Commun.* **2019**, *10*, 4663.
[45] D. J. Xue, J. H. Tan, J.-S. Hu, W. P. Hu, Y. G. Guo, L.-J. Wan, *Adv. Mater.* **2012**, *24*, 4528.
[46] L. J. Zhao, X. Li, L. L. Li, Y. P. Wu, T. Chen, Z. M. Wu, J. Y. Kang, *Phys. Status Solid-R* **2021**, *15*, 2100111.
[47] R. Zhang, X. Luo, F. Y. Zhao, Q. Xu, Y. Xu, Y. Xu, S. Chen, X. P. Fan, X. S. Qiao, *J. Solid State Chem.* **2022**, *310*, 123068.
[48] Y. Yu, Y. Ji, Z. Zhang, H. Qiao, Z. Y. Huang, X. Qi, Y. D. Liu, J. X. Zhong, *Ceram. Int.* **2021**, *47*, 17411.
[49] X. T. Wang, F. Zhong, J. Kang, C. Liu, M. Lei, L. F. Pan, H. L. Wang, F. Wang, Z. Q. Zhou, Y. Cui, K. H. Liu, J. L. Wang, G. Z. Shen, C. X. Shan, J. B. Li, W. D. Hu, Z. M. Wei, *Sci. China Mater.* **2020**, *64*, 1230.
[50] D. Wu, Y. G. Wang, L. H. Zeng, C. Jia, E. P. Wu, T. T. Xu, Z. F. Shi, Y. T. Tian, X. J. Li, Y. H. Tsang, *ACS Photonics* **2018**, *5*, 3820.
[51] D. Wu, C. G. Guo, L. H. Zeng, X. Y. Ren, Z. F. Shi, L. Wen, Q. Chen, M. Zhang, X. J. Li, C. X. Shan, J. S. Jie, *Light: Sci. Appl.* **2023**, *12*, 5.
[52] X. T. Wang, Y. T. Li, L. Huang, X.-W. Jiang, L. Jiang, H. L. Dong, Z. M. Wei, J. B. Li, W. P. Hu, *J. Am. Chem. Soc.* **2017**, *139*, 14976.
[53] Y. F. Xiong, Y. S. Wang, R. Z. Zhu, H. T. Xu, C. H. Wu, J. H. Chen, Y. Ma, Y. Liu, Y. Chen, K. Watanabe, T. Taniguchi, M. Z. Shi, X. H. Chen, Y. Q. Lu, P. Zhan, Y. F. Hao, F. Xu, *Sci. Adv.* **2022**, *8*, eabo0375.